Single-layer graphene modulates neuronal communication and augments membrane ion currents

Niccolò Paolo Pampaloni[1a], Martin Lottner[2a], Michele Giugliano[3,4,5], Alessia Matruglio[6b], Francesco D'Amico[7], Maurizio Prato[8,9,10], Josè Antonio Garrido[11,12*], Laura Ballerini[1*], Denis Scaini[1,7*]

[1] International School for Advanced Studies (SISSA), Trieste, Italy
[2] Walter Schottky Institut and Physik-Department, Technische Universität München, Am Coulombwall, Garching, Germany
[3] Molecular, Cellular, and Network Excitability, Department of Biomedical Sciences, Universiteit Antwerpen, Antwerpen, Belgium
[4] Department of Computer Science, University of Sheffield, S1 4DP Sheffield, UK
[5] Lab of Neural Microcircuitry, Brain Mind Institute, EPFL, CH-1015 Lausanne, Switzerland
[6] CNR-IOM - Istituto Officina dei Materiali, Area Science Park – Basovizza, S.S. 14 km 163,5 Trieste - Italy
[7] Elettra Sincrotrone Trieste S.C.p.A., S.S. 14 Km 163.5 in Area Science Park, I-34149 Trieste, Italy
[8]Department of Chemical and Pharmaceutical Sciences, University of Trieste, Trieste, Italy
[9]Nanobiotechnology Laboratory, CIC biomaGUNE, San Sebastiàn, Spain
[10]Ikerbasque, Basque Foundation for Science, Bilbao, Spain
[11]Catalan Institute of Nanoscience and Nanotechnology (ICN2), CSIC and The Barcelona Institute of Science and Technology, Campus UAB, Bellaterra, 08193 Barcelona, Spain
[12]ICREA, Pg. Lluís Companys 23, 08010 Barcelona, Spain

[a] these authors equally contributed to the work
[b] Present address: CERIC-ERIC (Central European Research Infrastructure Consortium), Area Science Park, Basovizza, S.S. 14 km 163,5 Trieste, Italy

Abstract

The use of graphene-based materials to engineer sophisticated bio-sensing interfaces adaptable to the central nervous system, requires a detailed comprehension of the behaviour of such materials in a biological context. Graphene peculiar properties may cause various cellular changes, but the underlying mechanisms remain unclear. Here, we show that single-layer graphene increases neuronal firing *via* altering membrane-associated functions in cultured cells. Graphene tunes the extracellular ions distribution at the interface with neurons, a key regulator of neuronal excitability. The resulting membrane biophysical changes include stronger potassium ion currents, with a significant shift in the fraction of neuronal firing phenotypes from *adapting* to *tonically firing*. By experimental and theoretical approaches we hypothesize that crucial to these effects are the graphene-ion interactions that are maximized when single layer graphene is deposited on electrically insulating substrates.

Graphene is a highly versatile two-dimensional nanomaterial widely adopted in many domains of science and technology, including advanced biomedical applications, due to its important electrical, optical and mechanical properties [1,2,3]. Its high carrier mobility and excellent optical transparency enable, for example, the design of novel transparent electrodes in optoelectronics [4]. Combining these features and, in particular, its remarkable electro-conductivity, makes graphene extremely appealing in neuroengineering, with reference to invasive implant technologies for brain biosensors and electrodes [5,6,7]. Despite the great interest and hopes raised by late development in graphene applications, the understanding of its functional

interactions with the brain tissue is still limited, particularly concerning the close proximity of a single plain layer of carbon atoms and the neuronal membrane ion fluxes in a biological milieu. So far, reports have shown that graphene-based materials can be safely interfaced with active neuronal cells [8,9,10], however an in-depth study on the influence of single-layer graphene (SLG) on the biophysics of neurons and *ex vivo* neuronal microcircuits upon is missing. In numerous electroceuticals applications [11,12], graphene is in contact with the extracellular environment that surrounds the excitable cell membranes. We thus asked: can SLG directly or indirectly alter neuronal activity? Which manipulations of graphene might be adopted to regulate *ad hoc* these interactions? Answering to these questions appears pivotal for future research in bio-hybrid electronic devices and, more in general, for providing insights on the deep interactions of technology with nature. Here, SLG obtained by chemical vapour deposition (CVD) was used to interface mammalian neurons, dissociated from the rat hippocampi, as a culture substrate. We employed different architectures of a single atomic layer graphene: (i) in contact with electrically-insulating/conductive substrates or (ii) suspended. By these arrangements, we studied the collective electrical activity of neuronal networks coupled on graphene and demonstrated that, when suspended, SLG increased neuronal excitability *via* inducing specific changes in membrane biophysics. These consist in a significant shift of the fraction of neuronal firing phenotypes from *adapting* to *tonically* firing. We then propose that graphene selectively modifies membrane-associated neuronal functions and hypothesize a specific interaction between graphene and cations, in particular potassium, in the extracellular solution crucially regulating cell excitability.

SLG potentiates cell signalling in neuronal networks

Large films of SLG and multi-layer graphene (MLG) were characterized by atomic force microscopy (AFM) and compared to glass pristine (Control) and gold-metalized (Au) glass samples (Fig. 1a). The quality of CVD-grown SLG and MLG samples was assessed by Raman and X-Ray photo-electron analysis. The recorded Raman spectra (Fig. 1b) supports the high quality of the SLG and MLG, by the low I_D/I_G ratios indicating a small amount of sp^3 hybridized carbon atoms at grain boundaries or binding surface moieties [13]. X-Ray photo-electron spectroscopy (XPS) analysis of SLG and MLG on Si_3N_4 reveals that both SLG and MLG samples contain a low degree of metal contamination (Fig. 1c).

To probe the electrical behaviour of excitable biological cells, we plated hippocampal neurons directly on graphene- and Au-coated coverslips. Recently, several reports described the successful growth of different cell types on graphene and graphene-based materials [9,14,15], but rarely investigating the *ex vivo* development and functional analysis of primary mammalian cells and neuronal microcircuits on uncoated monolayer of graphene. Neurons plated on glass coverslips were instead used as Control cultures [16,17,18]. SLG, MLG and Au substrates allow the growth of cells, with comparable mature morphology to Control (Fig. 2a). We further probed neuronal networks viability by quantifying network size and the ratio between neuronal and glial cells after 8-10 *days in vitro* (DIV), using immunofluorescence markers for neurons (class III β-tubulin) and astrocytes (GFAP). No differences were detected across all groups (Fig. 2b).

In culture, neurons develop functional synapses and display spontaneous collective electrical activity as a result of recurrent connections. We recorded spontaneous synaptic activity after 8÷10 DIV. This is indirectly informative of the combined effect

of existence, number, transfer gain of neuronal connections, and intensity of collective neuronal interactions. Heterogeneous post-synaptic currents (PSC, Supplementary Fig. 1b) were detected as inward currents of variable amplitudes [16] in all conditions, as shown in Figure 2c. While PSCs amplitude recorded from neurons growing on SLG, MLG and Au were similar to Control (top box plots in Fig. 2c) the PSCs frequency (bottom) was significantly higher in SLG than in other conditions. Instead, both MLG (chemically similar to SLG), and Au (chemically different but characterized by high electrical conductivity), did not affect the frequency of the synaptic events. The observed effect on PSCs is independent of the SLG film transfer-method used (Supplementary Fig. 1a). This suggests the mechanistic involvement of specific properties of the plain sheet of carbon atoms, in the modulation of PSCs frequency, but only when assembled as a monolayer. Miniature synaptic currents (mPSCs; Fig. 3a) were then recorded in a subset of Control and SLG neurons by further application of the fast-inactivating voltage-gated sodium channel blocker, tetrodotoxin (TTX, 1 μM), which impairs the action potentials (APs) and thus blocks network activity. Studying mPSCs allows disambiguating dynamical from structural components of the emerging network activity. In particular, mPSCs reflect the stochastic release of vesicles from the presynaptic terminals at individual synapses impinging onto the recorded neuron: their frequency depends on the pre-synaptic release probability and on the number of synaptic contacts, while their amplitude depends on postsynaptic receptor sensitivity [19]. As pointed out by the box plots in Figure 3a, we found significant difference neither in the frequency nor the amplitude of mPSCs, recorded in Control or SLG conditions. This suggests that the increased PSCs activity described earlier in SLG does not involve structural changes in the number or properties of synaptic

connections. This is further supported by immune-labelling experiments, where the number of VGlut1-positive *puncta*, used to label and identify glutamatergic presynaptic terminals [20], was not altered by the presence of SLG (Fig. 3b).

To rule out that SLG could interfere with the network composition or the maturation of inhibitory neurons, we carefully considered two alternative hypotheses. In the first one, the fraction of excitatory to inhibitory neurons is altered by SLG (e.g. in favour of the former), thus biasing the spontaneous network electrical activity detected as PSCs. We thus performed co-immunostaining with antibodies anti-class III β-tubulin and anti-GABA (Fig. 3c) and quantified the percentage of double-positive cells, indicating exclusively inhibitory neurons. In Control and SLG, we detected a comparable probability of finding double-positive cells (plot in Fig. 3c), thus ruling out SLG-induced alterations in the excitatory/inhibitory balance.

In the second hypothesis, SLG slows down the maturation of chloride ion fluxes through $GABA_A$ receptors. In neurons, the intracellular chloride concentration determines the amplitude of the inhibitory currents and, across successive developmental stages, shifts from higher to lower values, compared to the extracellular milieu [21]. Correspondingly, the activation of $GABA_A$ receptors results in a depolarizing (hyperpolarizing) drive of immature (mature) neurons [22]. We performed chloride imaging in living cells, using a quinoline-based Cl^- indicator dye: MQAE (N-[6-methoxyquinolyl] acetoethyl ester) [23]. As reported in Supplementary Fig. 2a, SLG had no impact in the GABAergic system maturation *in vitro*, a notion further supported by NKCC1 quantification (Supplementary Fig. 2b).

Thus, the SLG-mediated increase in neuronal signalling involve neither major network synaptic rearrangements, such as increased synaptogenesis or

(de)potentiation of synaptic efficacy, nor alterations in network composition or maturation of network inhibition.

To ultimately clarify the biophysical mechanisms leading to the boost in neuronal activity exhibited only by SLG, we examined directly single-cell excitability by current-clamp recordings. When Control and SLG neurons were hold at –60 mV in standard extracellular solution, an unbiased comparison of the basal AP frequency (Fig. 4a) could be obtained. Consistent with the PSC observations, we detected a significantly higher AP frequency in SLG neurons than in Control ones.

The subsequent bath addition of antagonists, selective for excitatory and inhibitory synaptic receptors, such as Gabazine (5 µM), CNQX (20 µM) and APV (50 µM), was employed to functionally decouple the recorded neurons from the synaptic network. Under these conditions, intrinsic neuronal active membrane properties were evaluated evoking AP responses by positive current pulses, delivered from the same resting potential (– 60 mV) [24,25]. When comparing the AP overshoot amplitude, half-amplitude width, threshold and maximal rising slope [25,26,27] in Control and SLG conditions no significant difference was found in the two groups (see Methods). All these considerations taken together suggest no major involvement of voltage-gated fast-inactivating Na^+ channel [27,28,29] in explaining the SLG-induced effects.

In addition, at –60 mV resting potential, under the cocktail of synaptic blockers, brief and sufficiently strong depolarizing pulses (2÷4 ms; 1 nA) easily evoked single APs in SLG and Control. The voltage trajectory of evoked single APs was followed by a transient after-hyperpolarizing (AHP) in SLG neurons, while only by a small after depolarization (ADP) in Control (Fig. 4b). When quantified in terms of the area below such trajectories, referred to the resting potential as baseline (histogram in Fig. 4b), the AHP in SLG neurons was significantly different than the

ADP detected in Control. Figure 4b shows the sensitivity of the AHP to various K^+ channel blockers. All these observations demonstrate that the AHP detected in SLG neurons was likely mediated by mixed K^+ conductances, including those activated by intracellular accumulation of free Ca^{++} [30,31]. The expression of these membrane channels is functionally related to spike-frequency adaptation, where sustained APs progressively slow-down over time. We then further examined the sustained discharge patterns of Control and SLG neurons, by injecting longer (1 s; 200 pA) depolarizing pulses (Fig. 4c and 4e). In the majority (81.8%; Fig. 4d) of Control neurons, sustained AP firing was dominated by spike frequency adaptation, which we named *adapting* discharge phenotype. This often resulted in an early burst of closely spaced APs, followed by a progressive decay of AP amplitudes, leading to adaptation. On the contrary, SLG neurons (83.3%; Fig. 4d) showed no APs adaptation, which we named *tonic* discharge phenotype, where cells fired continuously and more regularly without apparent accommodation [32,33]. Taken together, these data hint at a complex homeostasis in the K^+ currents expressed by neurons when coupled to SLG substrates. This hypothesis was reinforced by results obtained under voltage-clamp in control and SLG neurons, where depolarizing voltage pulses starting from a –60 mV holding potential baseline evoked an outward current (Fig. 4f), presumably due to the activation of a mixed population of K^+ channels. When examined under these conditions, SLG neurons were characterized by a significantly larger outward current at positive potentials, shown in the steady-state current/voltage (I/V) plot of Figure 4f, likely consequence of an up-regulation of mixed K^+ currents. This evidence taken together strongly indicates that SLG substrates induce active changes in the electrical properties of growing neurons, presumably related to altered homeostasis of K^+ membrane currents and leading to a

modulation of the single-cell firing phenotypes and ultimately to an increased network activity. Importantly, SLG neurons generated more APs when compared to Controls, even in response to milder and shorter stimuli (Supplementary Fig. 3a and b).

The observed correlations between single-cell properties, resulting phenotype, and network effects were further investigated by mathematical modelling. We addressed the causality between neuronal firing patterns and network activity, by examining a spike-rate model of the electrical activity emerging in populations of cultured neurons with recurrent synaptic connections (Fig. 5a).

We simulated a network of 1600 neurons with a fraction of excitatory to inhibitory neurons equal to 80/20 as *in vitro* (Fig. 3c) [34]. Since inhibitory cells usually display a tonic electrical phenotype only, we hypothesized that the change in the ratio between adapting and tonically firing neurons observed in our experiments, occurred in excitatory cells only. We therefore modelled two subpopulations of excitatory neurons: one with *adapting* and the other with *tonic* phenotypes. We found that the higher the relative fraction of *tonic* firing neurons, the higher the rate of occurrence of synchronized bursts (Fig. 5b and 5c). This supports the conclusion that the observed increase in the frequency of spontaneous (PSCs/APs) activity (Fig. 2c, SLG) is caused by the different ratio of cells with adapting/non-adapting phenotypes.

The potassium ions hypothesis

By a biophysical model, we tested *in silico* two mutually non-exclusive hypotheses for the observed changes in single-cell firing phenotype: (i) an increase in the total outward ionic conductance or, alternatively, (ii) a modest depletion in the extracellular concentration of K^+ ions. The rationale behind these single-cell

simulations is that either SLG induced a chronic increase in ion currents involved in firing regulation, or SLG acutely altered cell firing by changing ion mobility.

In our model, by stripping down cell excitability to its bare essential, we explored whether stronger outward potassium currents favours excitability and not always oppose to it, as intuitively expected. We found that the progressive sodium current inactivation (Fig. 5d, lower left, green traces) – occurring for simplicity in the model only over *fast* and not slow time scales – could be counterbalanced and reversed by strong K^+ currents (Fig. 5d, lower right, red traces). This results in a sustained, tonic, response to an external current stimulus (i.e. compare Fig. 5d to 4c), instead of a progressive firing inactivation. While this effect is reversed by simulating an overexpression of Na^+ channels (e.g. at the axon initial segment), it serves us here as a proof of concept of a counter-intuitive phenomenon: increasing outward currents increases cellular excitability, by removing sodium current inactivation. Of course, an *ad hoc* increase in the maximal conductance of sodium ion channels also increases excitability, although – in the model – with distinct features in the type of transition associated to the *limit cycle* to sustained AP firing (Supplementary Fig. 4). Therefore, in the model the more K^+ channels the higher the excitability, in those regimes where progressive sodium inactivation affects firing (Fig. 5e).

Outward K^+ currents also depend on the ionic driving force beyond on the maximal conductance (i.e. $I_K \sim G_K\ (E_K - V)$ - see Methods), so that in theory a change in the local ionic composition might reverse sodium inactivation too. In fact, the Nernst equilibrium potential E_K depends on the K^+ concentrations outside and inside the membranes [35]. Should SLG interfere extracellularly with K^+ bulk diffusion in its proximity (see below) then a depletion of K^+ (e.g. 10-20%, as $[K^+]_{EX} \rightarrow \delta \cdot [K^+]_{EX}$, $\delta = 0.8 - 0.9$), would lead to an increase in the ionic driving force, as E_K would decrease

accordingly (i.e. ~2-5 mV). By simulations (Fig. 5f), we found that a modest decrease in E_K (e.g. from –75 to –77.6 mV) could indeed counterbalance sodium inactivation, at least for an intermediate external stimulus intensity and without altering significantly the resting membrane potential.

We thus speculate that changes in excitability of cells coupled to SLG might be caused by an extracellular reduced mobility of K^+ at the interface between the nanomaterial and the solution, leading to a K^+ depletion at the neuronal membranes.

Localized potassium ions depletion in cell-substrate cleft

We hypothesize that at the core of SLG ability to alter neuronal excitability is the ion adsorption on graphene surfaces. This may result in a modification of ion mobility, in particular K^+, at the neuronal/graphene interface.

Within this proposed mechanism, it is still unclear how SLG might modify K^+ ion mobility while MLG (or Au) do not. It is well known that carbon-based π electron-rich surfaces show a significant surface enrichment of cations in ionic solutions, due to specific cation-π interactions [36,37,38,39]. Because of its size, in solution, K^+ ions are weaklier solvated by water, when compared to other species (e.g. Li^+ or Na^+ ions) but are still good π binders. This feature makes K^+ the best alkali metal binder to carbon-based surfaces in aqueous solutions [38,39]. This implies that, in nanoscale-confined systems, cation trapping occurring at the carbon surface level may lead to a significant local depletion of ions, in particular potassium, at the neuronal membrane surface level.

Addressing this point, Raman spectroscopy (sketched in Supplementary Fig. 5a) was performed on supported SLG and MLG samples in liquid condition without and in the presence of KCl and NaCl at physiological concentrations (4 mM and 150 mM,

respectively) in the solution. SLG Raman G-peak exhibited a change in shape and position in the presence of NaCl and KCl D_2O solutions (Fig. 6a, left, inset) while in MLG it did not change (Fig. 6a, right, inset). The mechanisms responsible for the observed shift in the G Raman band of graphene with, more importantly, the narrowing of the G band (FWHM) detected in SLG when samples are immersed in a KCl solution could result from charge doping [40] or internal strain [41]. More specifically, the shifts in G-band position exhibited by SLG in the presence of salt solutions could be indicative of a specific cation interaction, not measurable in MLG. Notably, the larger G-band Raman shift in KCl-treated samples (3 ± 0.5 cm^{-1}) than in the presence of NaCl (1 ± 0.5 cm^{-1}) correlates well with a larger SLG affinity for hydrated K^+ when compared to Na^+.

Importantly, in our experimental settings, the specific cation-π interaction at surface level could result in partial K^+ depletion from the extracellular solution facing the cell membrane (Fig. 6b) due to the tiny thickness of the cleft (see Supplementary Information and Fig. S6) between cells and substrates.

Substrate modulation of graphene cation-π interaction

Our experiments have shown that SLG behaves differently from MLG in respect to the K^+ homeostasis of neurons and subsequent improved excitability. The two nanomaterials culturing platforms, SLG and MLG, differ only in the conductive properties of the supporting structure immediately below the first mono-atomic carbon layer exposed to the biological milieu (i.e., on one hand glass and on the other multiple layers of graphene/graphite). From the point of view of a neuron growing on its top, MLG appears as a SLG film layered on the underlying, electrically

conductive, MLG. In our hypothesis, graphene efficiency in trapping K^+ ions is tuned or influenced by the electronic properties of the supporting structure [42,43].

In this framework, we compared PSCs in neurons directly grown on glass (Control), on free-standing SLG (suspended SLG, see Methods) and on SLG transferred on an insulating substrate (SLG on glass) and on a conductive substrate of Indium Tin-Oxide (SLG on ITO)[18]. The results of such experiments (Figure 6c) are in full agreement with our hypothesis: the PSCs frequency was boosted by SLG on glass, and even more by suspended SLG, with no detectable effects when SLG was layered on ITO. Notably, in suspended SLG, PSCs amplitude is also significantly higher than Control.

It is not trivial to understand the underlying exact mechanism, in the absence of any theoretical model describing the dependency of graphene π-cation interaction on supporting surface properties, we speculate that surface conductivity is playing a key role. In particular, in suspended SLG, environmental disturbances are minimized allowing access to the intrinsic properties of graphene close to the unperturbed Dirac point. Superficial charge inhomogeneity is reduced in this case compared to supported samples, giving rise to a “close-to-theory” system [1,44] (Fig. 6d, left) that will fit better to cation-π simulations’ results [33,45,46]. SLG laying on metal surfaces usually undergo electron-doping resulting in a down-shift of graphene Dirac point [47] (Fig. 6d, middle). This will induce a homogeneous charge-distribution [48] that could result in a reduction of graphene cation-π interaction force. On the other hand, in SLG transferred on insulating substrates there are significant local fluctuations in surface potential [49,50], thus inducing an inhomogeneous charge distribution on graphene surface where neutral areas, where SLG band structure is basically unperturbed as in the case of suspended graphene, and p-doped areas, coexist

[51,52]. In the latter case, graphene-K^+ interactions will still be present even if with less pronounced effect than on suspended SLG. Our preliminary Raman results can explain the different behaviour of SLG towards K^+ or Na^+ and the difference between SLG and MLG behaviour in ion solution. However, they do not directly demonstrate differences between SLG and MLG in ion absorbance.

Conclusions

SLG modifies neuronal excitability and we propose that this effect is mediated by graphene ability to restrict K^+ ions mobility in close proximity to the material surface, but only when the monolayer is deposited on electrically insulating substrates. We cannot exclude additional mechanisms related to non-uniform charge carrier densities, affecting surface concentrations of ions [53]. Alternatively, restricted ion mobility might affect the way astrocytes regulate the extracellular *milieu* between graphene and neurons.

Ultimately, we provided multiple lines of evidence to demonstrate that SLG, when engineered on an insulating glass-substrate, is able to tune neuronal excitability. Our physiological experiments demonstrate that the detected increase in neuronal synaptic activity is caused by increased cell firing, rather than by changes in network size, synaptic density [54,55,56], inhibition/excitation ratio or inhibition maturation. We also demonstrated that neurons, exposed to SLG, up-regulate K^+ currents and switch to functionally-tonic firing phenotypes. Our simulations support the notion that changes in the ratio of adapting/firing neurons will impact the global network activity [57,58] and suggest the key contribution of up-regulated potassium currents in driving this change. All these effects are not mimicked by MLG or other conductive substrates, such as Au. We propose that, due to the cation-π interactions of

graphene, cations, and K^+ in particular [37,38,39], will be trapped at the graphene surface, resulting in a graded ionic depletion at distances from the material compatible with the nanometre-scale characterizing cell-adhesion mechanisms [59,60]. This hypothesis is grounded in earlier molecular dynamics simulations at the equilibrium [37], where ionic enrichment occurs at the interface.

Graphene properties might thus affect neuronal information processing *in virtue* of the physical interactions of such a nanomaterial with the biological environment. Novel materials might then represent, in general, unconventional tools to gain insights into genuine biological processes.

REFERENCES

[1] Novoselov, K. S. et al. Electric Field Effect in Atomically Thin Carbon Films. Science 306, 666-669 (2004).

[2] Geim, A. K. & Novoselov, K. S. The rise of graphene. Nat Mater. 6, 183-191 (2007).

[3] Yang, Y. et al. Graphene based materials for biomedical applications. Mat Today 16, 365-373 (2013).

[4] Li, X., et al. Transfer of large-area graphene films for high-performance transparent conductive electrodes. Nano Lett. 9, 4359-4363 (2009)

[5] Shin, S. R. et al. Graphene-based materials for tissue engineering. Adv Drug Deliv Rev. 105, 255-274 (2016).

[6] Lu, Y. et al. Flexible Neural Electrode Array Based-on Porous Graphene for Cortical Microstimulation and Sensing. Sci Rep. 6, 33526 (2016).

[7] Herbert, C. et al. Flexible graphene solution-gated field effect transistors, efficient transducers for micro-electrocorticography Adv. Funct. Mater.28, 1703976 (2017).

[8] Kim, J. et al. Monolayer Graphene-Directed Growth and Neuronal Differentiation of Mesenchymal Stem Cells. J Biomed Nanotechnol. 11, 2024-2033 (2015).

[9] Fabbro, A. et al. Graphene-Based Interfaces Do Not Alter Target Nerve Cells. ACS Nano 10, 615-623 (2016).

[10] Rauti, R. et al. Graphene Oxide Nanosheets Reshape Synaptic Function in Cultured Brain Networks. ACS Nano 10, 4459-4471 (2016).

[11] Famm, K. et al. Drug discovery: a jump-start for electroceuticals. Nature 496, 159-161 (2013).

[12] Rivnay, J. et al. Next-generation probes, particles, and proteins for neural interfacing. Sci Adv. 3, e1601649 (2017).

[13] Cançado, L.G. et al. Quantifying defects in graphene via Raman spectroscopy at different excitation energies. Nano Lett. 11, 3190-3196 (2011).

[14] Kim, J. et al, Monolayer Graphene-Directed Growth and Neuronal Differentiation of Mesenchymal Stem Cells. J Biomed. Nanotechnol. 11, 2024-2033 (2015).

[15] Baldrighi, M. et al, Carbon Nanomaterials Interfacing with Neurons: An In vivo Perspective. Front. Neurosci. 10, 250 (2016).

[16] Lovat, V. et al. Carbon nanotube substrates boost neuronal electrical signaling. Nano Lett. 5, 1107-1110 (2005).

[17] Cellot, G. et al. Carbon nanotubes might improve neuronal performance by favouring electrical shortcuts. Nat. Nanotechnol. 4, 126-133 (2009).

[18] Cellot, G. et al, Carbon nanotube scaffolds tune synaptic strength in cultured neural circuits: novel frontiers in nanomaterial-tissue interactions. J. Neurosci. 31, 12945-12953 (2011).

[19] Raastad, M. et al. Putative Single Quantum and Single Fibre Excitatory Postsynaptic Currents Show Similar Amplitude Range and Variability in Rat Hippocampal Slices. Eur J Neurosci. 4, 113-117 (1992).

[20] Pampaloni, NP. et al. Sculpting neurotransmission during synaptic development by 2D nanostructured interfaces. Nanomedicine. S1549-9634, 30082-5 (2017).

[21] Arosio, D. & Ratto, GM. Twenty years of fluorescence imaging of intracellular chloride. Front Cell Neurosci. 8, 258 (2014).

[22] Cherubini, E. GABA mediated excitation in immature rat CA3 hippocampal neurons. Int J Dev Neurosci. 8, 481-90 (1990).

[23] Marandi, N., Konnerth, A. & Garaschuk O. Two-photon chloride imaging in neurons of brain slices. Pflugers Arch. 445, 357-65 (2002).

[24] Ruscheweyh, R. & Sandkuhler, J. Lamina-specific membrane and discharge properties of rat spinal dorsal horn neurones in vitro. J Physiol. 541, 231-244 (2002).

[25] Chang, YM. & Luebke, JI. Electrophysiological diversity of layer 5 pyramidal cells in the prefrontal cortex of the rhesus monkey: in vitro slice studies. J Neurophysiol. 98, 2622-32. (2007)

[26] Routh, B. N. et al. Anatomical and Electrophysiological Comparison of CA1 Pyramidal Neurons of the Rat and Mouse. J Neurophysiol. 102, 2288–2302 (2009).

[27] Renganathan, M., Cummins, TR. & Waxman, SG. Contribution of Na(v)1.8 sodium channels to action potential electrogenesis in DRG neurons. J Neurophysiol. 86, 629-40 (2001).

[28] Platkiewicz, J. & Brette, R. Impact of Fast Sodium Channel Inactivation on Spike Threshold Dynamics and Synaptic Integration. PLoS Comput Biol. 7, e1001129 (2011).

[29] Kress, G. J. et al. Axonal sodium channel distribution shapes the depolarized action potential threshold of dentate granule neurons. Hippocampus 20, 558-571 (2016).

[30] Storm, J. F. Action potential repolarization and a fast after-hyperpolarization in rat hippocampal pyramidal cells. J Physiol. 385, 733-759 (1987).

[31] Sah, P. & Faber, E. S. Channels underlying neuronal calcium-activated potassium currents. Prog Neurobiol. 66, 345-353 (2002).

[32] Dégenètais, E. et al. Electrophysiological properties of pyramidal neurons in the rat prefrontal cortex: an in vivo intracellular recording study. Cereb Cortex 12, 1-16 (2002).

[33] Furlan, F. et al. ERG conductance expression modulates the excitability of ventral horn GABAergic interneurons that control rhythmic oscillations in the developing mouse spinal cord. J. Neurosci. 27, 919-928 (2007).

[34] Marom, S. & Shahaf, G. Development, learning and memory in large random networks of cortical neurons: lessons beyond anatomy. Q Rev Biophys. 35, 63-87 (2002).

[35] Sterratt, D. Principles of computational modelling in neuroscience. Cambridge University Press(2011).

[36] Kumpf R A, & Dougherty D A. A mechanism for ion selectivity in potassium channels: computational studies of cation-pi interactions. Science. 261, 1708-10 (1993).

[37] Shi, G, et al. Ion enrichment on the hydrophobic carbon-based surface in aqueous salt solutions due to cation-π interactions. Sci Rep., 3, 3436 (2013).

[38] Pham T A, et al. Salt Solutions in Carbon Nanotubes: The Role of Cation−π Interactions J. Phys. Chem. C, 120, 7332-7338 (2016).

[39] Williams, C D, et al. Effective Polarization in Pairwise Potentials at the Graphene–Electrolyte Interface J. Phys. Chem. Lett., 8, 703-708 (2017)

[40] Dong, X et al. Doping single-layer graphene with aromatic molecules. Small. 5, 1422-6 (2009)

[41] Chacón-Torres, JC, Wirtz, L, Pichler, T. Manifestation of charged and strained graphene layers in the Raman response of graphite intercalation compounds. ACS Nano. 7, 9249-59 (2013).

[42] Novák M, et al. Solvent effects on ion-receptor interactions in the presence of an external electric field. Phys Chem Chem Phys. 18, 30754-30760 (2016).

[43] Chen, K. et al, Electronic Properties of Graphene Altered by Substrate Surface Chemistry and Externally Applied Electric Field. J. Phys. Chem. C, 116, 6259-6267 (2012)

[44] Novoselov, K. et al., Two-dimensional gas of massless Dirac fermions in graphene. Nature. 438, 197-200 (2005).

[45] Gigante, G. et al. Network Events on Multiple Space and Time Scales in Cultured Neural Networks and in a Stochastic Rate Model. PLoS Comput Biol. 11, e1004547 (2015).

[46] Gambazzi, L. et al. Diminished activity-dependent brain-derived neurotrophic factor expression underlies cortical neuron microcircuit hypoconnectivity resulting from exposure to mutant huntingtin fragments. J. Pharmacol Exp Ther. 335, 13-22 (2010).

[47] González-Herrero, H et al. Graphene Tunable Transparency to Tunneling Electrons: A Direct Tool to Measure the Local Coupling. ACS Nano. 10, 5131-44 (2016).

[48] Praveen, C. S. et al., Adsorption of alkali adatoms on graphene supported by the Au/Ni(111) surface, Phys Rev. B 92, 075403 (2015).

[49] Kang, Y-J. et al. Electronic structure of graphene and doping effect on SiO_2 Phys Rev. B 78, 115404 (2008).

[50] Miwa, R. H. et al. Doping of graphene adsorbed on the a-SiO_2 surface. Appl Phys Lett 99, 163108 (2011).

[51] Ao, Z. et al. Density functional theory calculations on graphene/α-SiO2(0001) interface. Nanoscale Res Lett. 7, 158 (2012).

[52] Fan, X. F. et al. Interaction between graphene and the surface of SiO_2. J Phys Condens Matter. 24, 305004 (2012).

[53] Hille, B. Ion channels of excitable membranes. Sunderland, Mass: Sinauer, (2001).

[54] Slomowitz, E. et al. Interplay between population firing stability and single neuron dynamics in hippocampal networks. eLife 4, e04378 (2015).

[55] Bogaard, A. et al. Interaction of cellular and network mechanisms in spatiotemporal pattern formation in neuronal networks. J Neurosci. 29, 1677-1687 (2009).

[56] Sahasranamam, A. et al. Dynamical state of the network determines the efficacy of single neuron properties in shaping the network activity. Sci Rep. 6, 26029 (2016).

[57] Radulescu, R.A. Mechanisms Explaining Transitions between Tonic and Phasic Firing in Neuronal Populations as Predicted by a Low Dimensional Firing Rate Model. PLoS One 5, e12695 (2010).

[58] Naud, R. et al. Firing patterns in the adaptive exponential integrate-and-fire model. Biol Cybern. 99, 335-347 (2008).

[59] Wrobel G, Höller M, Ingebrandt S, Dieluweit S, Sommerhage F, Bochem HP, Offenhäusser A. Transmission electron microscopy study of the cell-sensor interface. J R Soc Interface. 5, 213-222. (2008).

[60] Braun, D. & Fromherz, P. Fluorescence interference-contrast microscopy of cell adhesion on oxidized silicon. Appl Phys A 65, 341-348 (1997).

[61] Ferrari A. C. et al. Raman spectrum of graphene and graphene layers. Phys. Rev. Lett. 97, 187401 (2006).

[62] Cançado, L. G. et al. Measuring the degree of stacking order in graphite by Raman spectroscopy. Carbon 46, 272-275 (2008).

[63] Alagem, N. et al, Mechanism of Ba(2+) block of a mouse inwardly rectifying K+ channel: differential contribution by two discrete residues. J Physiol. 534, 381-393 (2001).

[64] Alger, B. E. & Nicoll, R. A. Epileptiform burst afterhyperolarization: calcium-dependent potassium potential in hippocampal CA1 pyramidal cells. Science 210, 1122-1124 (1980).

[65] Jiang, Y. & MacKinnon, R. The barium site in a potassium channel by x-ray crystallography. J Gen Physiol. 115, 269-272 (2000).

[66] Nisenmbaum, E. S. & Wilson, C. J. Potassium currents responsible for inward and outward rectification in rat neostriatal spiny projection neurons. J Neurosci. 15, 4449-4463 (1995).

[67] Pisirowski, R. & Aldrich, R. W. Calcium activation of BK(Ca) potassium channels lacking the calcium bowl and RCK domains. Nature. 420, 499-502 (2002).

[68] Stocker, M. et al, An apamin-sensitive Ca^{2+}-activated K^{+} current in hippocampal pyramidal neurons. Prot Nat Acad Sci. 96, 4662-4667(1999).

[69] Hodgkin, A. L. & Huxley, A. F. A quantitative description of membrane current and its application to conduction and excitation in nerve. J Physiol. 117, 500-544 (1952).

[70] French, C. R. et al. Properties of an intermediate-duration inactivation process of the voltage-gated sodium conductance in rat hippocampal CA1 neurons. J Neurophysiol. 115, 790-802 (2016).

Acknowledgement

We are grateful to M. Lazzarino and S. Dal Zilio for experimental assistance in the fabrication of suspended SLG and FIB analysis; N. Secomandi and R. Rauti for assistance in imaging. We thank A. Laio, G. Scoles, A. Nistri and B. Cortés-Llanos for helpful discussion. This paper is based on work supported by the European Union Seventh Framework Program under grant agreement no. 696656 Graphene Flagship and no. 720270 Human Brain Project Flagship, and by the Flanders Research Foundation (grant no. G0F1517N). MP, as the recipient of the AXA Chair, is grateful to the AXA Research Fund for financial support. MP was also supported by the Spanish Ministry of Economy and

Competitiveness MINECO (project CTQ2016-76721-R), by the University of Trieste and by Diputación Foral de Gipuzkoa program Red (101).

Author Contributions

N.P.P. performed electrophysiological experiments, imaging, immunochemistry, confocal microscopy and all the related analysis; M.L. fabricated supported SLG and MLG and performed all material characterization; M.G. performed mathematical simulations and analysis and contributed to the writing of the manuscript; A.M. fabricate suspended SLG and gold plated samples; F.D.A. and A.M. performed Raman experiments and data analysis on SLG and MLG in wet and dried conditions; M. P., D.S. and L.B. conceived the study; D.S., L.B., and J.A.G. designed the experimental strategy, interpreted the results and wrote the manuscript.

Competing financial interests

The authors declare no competing financial interests.

FIGURE LEGENDS

Figure 1 | Characterization of the substrates. a, AFM topography reconstructions of glass control, SLG, MLG and gold plated glass surfaces. AFM documented a surface roughness of the materials that varied from 0.23 ± 0.02 nm in Control (n = 3 sample), 1.5 ± 0.5 nm in SLG (n = 3 sample), 20 ± 10 nm for MLG (n = 3 sample) and 0.47 ± 0.1 nm for Au (n = 3 sample). Scale bar: 5 μm. **b**, Spatial maps of the 2D/G and D/G peak amplitude ratio maps. Scale bar: 10 μm. The single punctual

Raman spectra of SLG (in red) and MLG (in blue) represent mapping data points with the corresponding average peak amplitude ratios. On the right, relative spatial 2D/G and D/G ratio maps. The FWHM of the 2D peak, as well as the I_{2D}/I_G ratio are indicative of a low bilayer content in the case of SLG [61] and turbostratic graphite in the case of MLG [62]. A graphitic Raman signature is to be expected as the MLG samples have a typical thickness of a few hundreds of layers. **c**, XPS spectrum (X-Ray source: Mg Kα) of SLG (in red) and MLG (in blue). Dotted lines highlight the relevant elements, while the unlabelled features around 750 eV and 980 eV correspond to the oxygen KL_1L_1 and the carbon KVV Auger lines respectively.

Figure 2 | Single-Layer graphene increase neuronal network activity. a, Representative SEM micrographs depicting hippocampal neurons morphology after 10 DIV, supported by the different substrates (n = 5 fields each). Culture substrates were not pre-treated with any additional adhesion molecules, which might mask the effects of graphene. Scale bar: 10 μm. **b**, Representative fluorescent microscopy images showing dissociated hippocampal networks labelled with class III β-tubulin (for neurons) in red and GFAP (for astrocytes) in green. Scale bar: 100 μm.
The histograms show the density of cells (top) and the neuron/glia ratio (bottom) across all four conditions, which did not significantly differ (n = 30 fields, 3 culture series each). In addition, SLG or MLG topography did not influence neuronal fibres' orientation in respect to Control or Au (see Methods). These observations, combined to the similarity of membrane passive electrical properties (see Methods), indicated the homogeneous growth of healthy neurons [17] across substrates, with comparable levels of cellular composition and organization. **c**, Representative traces of the spontaneous network activity of neurons grown on the different substrates are

shown (left), the corresponding isolated PSCs are shown superimposed (middle; in black the average values). Box plots summarize the PSC amplitude values (right, top) and the PSC frequency ones (right, bottom) in all experimental conditions (SLG, n = 45; MLG, n = 20; Au, n = 20; Control, n = 40). Note the significantly higher PSC frequency in SLG than all other substrates (i.e., Control 1.53 ± 0.22 Hz; SLG 3.21 ± 0.41 Hz; P=0.0010). Differences between the variables were assessed using one-way ANOVA and multiple comparisons were adjusted by Bonferroni correction.

Figure 3 | Single-layer graphene does not increase the number of synapses and the network composition. a, Exemplificative traces of spontaneous synaptic activity, recorded in the presence of TTX, are shown together with their superimposed mPSCs (right, in black the average values). Control (n = 11) and SLG (n = 11) mPSC frequency and amplitude are summarized in the box plots, note that no differences were detected in these parameters. **b**, Confocal images of neuronal cultures (10 DIV) in Control and SLG identifying the presynaptic VGlut1 (in green) in III β-tubulin positive cells (orange). Scale bar: 20 μm. Higher magnifications of the region highlighted by white boxes are displayed for clarity. Scale bar: 5 μm. The histograms on the right summarize VGlut1 puncta densities in the two conditions (5.2 ± 1.14 in Control and 4.5 ± 0.64 in SLG; P = 0.207, n = 30 fields, 3 cultures each). **c**, Confocal images of neuronal cultures (10 DIV) in Control and SLG identifying positive cells for class III β-tubulin and GABA. Scale bar: 10 μm. The histograms on the right summarize the percentage of double-positive cells in the two conditions (33 ± 2.7 % in Control and 30 ± 2.5 % in SLG; P = 0.21, n= 20 fields each). Statistically significant difference between two data sets was assessed by Student's t test for parametric data and by Mann-Whitney for non-parametric ones.

Figure 4 | SLG triggers changes in single cell intrinsic excitability. a, Representative current-clamp recordings of hippocampal neurons in culture (10 DIV) in Control and SLG. Control and SLG neurons displayed similar resting membrane potentials (–52 ± 10 mV in SLG; –50 ± 7 mV in Control). When hold at –60 mV, the cell's spontaneous AP firing was measured as summarized in the histograms (right). Note the significantly higher AP frequency in SLG (2.60 ± 0.36 Hz in SLG, n = 21; 1.37 ± 0.26 Hz in Control, n = 19; P = 0.0054). **b**, Evoked single AP in Control (top) and SLG (bottom). Note the pronounced AHP in SLG neurons, that was partially abolished by each of the treatments shown: BaCl, TEA or Apamin (right, superimposed tracings). The histogram quantifies the area below the Control and SLG post-AP voltage trajectories with respect to the resting membrane potential. The AHP in SLG neurons was significantly different than the ADP detected in control neurons (–86.96 ± 23.60 mV·ms in SLG, n = 25; +107.12 ± 21.85 mV·ms in Control, n = 20; P = 0.0010). Interestingly, the AHP was reduced (by 88%) by bath applying Ba^{++} ($BaCl_2$, 2 mM; n = 3), which is known to block K_{ir} and K_{Ca} membrane channels [63,64,65,66]. The AHP was also reduced (by 58%) by bath applying tetra-ethylammonium (TEA, 1 mM; n = 9) a non-selective blocker of the large majority of voltage gated K^+ membrane channels (K_v) [30], including BK_{Ca} channels [67]. Finally, Apamin (200 µM; n = 5), a specific inhibitor of SK_{Ca} membrane channels [68], also strongly affected (47% reduction) the AHP. **c**, Current-clamp recordings from neurons in control and SLG revealed different cell discharge patterns, classified as *adapting* or *tonic*. **d**, Bar charts illustrate probability distributions (expressed as percentage of sampled population) of each cell type in Control (n = 13) and SLG (n = 15) cultures. Note that in Control 81.8% are *adapting* and in SLG 83.3% are *tonic*. **e**,

Scatter plot of after-potential area *vs*. the number of action potentials (APs) in SLG neurons when a single AP is elicited (as in b; open circle) or when multiple APs are evoked (as in c, filled circle) by 1 s long depolarizing step (–352 ± 70 mV·ms upon long depolarizing steps). **f**, Representative records of voltage-activated outward currents evoked by depolarizing current steps in Control and SLG (capacitive transients were not removed). Plot summarizes the I/V relation in Control (n = 13) and SLG (n = 15) neurons obtained upon subtraction of leak currents. Note that SLG outward currents were significantly larger than control ones (10 mV step, P=0.032; 20 mV step, P=0.031; 30 mV step, P=0.019). Statistically significant difference between two parametric data sets was assessed by Student's t test.

Figure 5 | Spike-rate network model. The electrical activity of excitatory and inhibitory recurrently interacting neurons was described by a mathematical model (see Supplemental Methods). **a**, The increase in the fraction of non-adapting neurons, observed *in vitro* on graphene substrates, predicts a higher rate of occurrence *in silic*o for spontaneous “bursts” of spikes, synchronized across the network. These bursts are presynaptic correlates of the synaptic potentials, observed experimentally by voltage-clamp. **b** and **c**, Samples of the simulated network firing rates, analysed in **a**, are shown for two fractions of non-adapting neurons, *i.e.* 20% and 80%, out of the total of excitatory neurons. **d**, Counter-intuitive effects of outward potassium currents on cell excitability are explored in a single-cell biophysical model (parameters as in Table 2). As a proof of concept, we considered the simplest possible model of AP generation, as proposed by Hodgkin and Huxley (HH) [69]. This model describes the generation of a (train of) AP(s) in terms of the known

interplay between fast-inactivating (~1 ms) inward Na^+ currents and delayed rectifier outward K^+ potassium currents –of course, by no means these are the only membrane currents underlying the electrophysiological behaviour of rat hippocampal neurons [70]. The membrane potential responses (black traces) to an external step current was simulated, as in the experiments (see Methods). **d** and **e**, Plots within each panel exemplify how an increase (from left to right subpanels) of the maximal K^+ conductance or, in **f**, its driving force, through a depletion of extracellular K^+ ions, may to some extent reverse the inactivation of inward Na^+ currents (green traces in **d**). Then, inactivating neuronal responses may turn into sustained firing thereby increasing cell excitability (as in **c**). All in all, this suggests a specific involvement of the extracellular concentration of K^+ in neuronal excitability: the less extracellular K^+ the higher the excitability, at least in those regimes where progressive sodium inactivation affects neuronal firing disfavoring sustained *tonic* response. Parameters: in **d**, G_K in {0.012; 0.0216} mS/mm^2; in **e**, G_K in {0.012, 0.04, 0.06} mS/mm^2 from left to right, I_{stim} 5 nA/mm^2; in **f**, I_{stim} as in **e**, while E_K in {-75, -77.6, -80.5} mV from left to right, corresponding to a {0%, 10%, 20%} depletion of extracellular K^+ ions.

Figure 6 | Graphene deplete potassium at the cell/substrate cleft. a, Graphene-related G vibrational peak [61] was evaluated in wave number position for both SLG (left) and MLG substrates (right) with samples totally immersed in pure deuterium oxide (D_2O), in D_2O solution containing 4 mM KCl, and in D_2O solution containing 150 mM NaCl (see Supplementary Methods for technical details). The wavenumber maximum position relative to the G-peak Raman shift for control SLG sample was collocated at 1599 ± 0.5 cm^{-1}. It exhibited a change in shape associated to a G-peak position shift to 1600 ± 0.5 cm^{-1} and to 1602 ± 0.5 cm^{-1} in the presence of NaCl and

KCl D_2O solutions, respectively (left, inset). Conversely, in MLG samples G peak maximum position did not change (right, inset). **b**, Sketch of the local amount of K^+ depletion in the membrane/surface cleft due to graphene trapping as function of cleft thickness. In light green the extrapolated values of such a distance (40÷100 nm) [34]. See Supplementary methods for technical details. **c**, Box plots summarize the average PSC frequency values (left) and the average PSC amplitudes ones (right) for neurons developed on glass control (in grey, n = 21), on glass supported SLG (in red, n = 21), on free-standing SLG (in green, n = 26) and on SLG deposited on ITO (in blue, n = 8). Note the significant increase in PSC frequency in SLG laying on insulating glass than Controls (3.11 ± 0.35 Hz vs. 1.72 ± 0.21 Hz, P = 0.031) or, even more, when grown on suspended SLG (4.22 ± 0.35 Hz vs. Controls, P = 0.001). SLG on conductive ITO does not change neuronal activity. Notably, in suspended SLG, PSCs amplitude is also significantly increased (59.2 ± 5.8 pA *vs.* 35.9 ± 4.9 pA, P = 0.017) when compared to control cultures. **d**, Hypothesis of Dirac point and Fermi level rearrangement as function of SLG supporting material (bottom), and an exemplification of the possible charge distribution in graphene layer as function of electrical characteristics of the underlying surface (top). Blue areas represent more positive regions (e.g. depletion of electrons), red areas represent more negative ones (e.g. persistency of electrons).

Differences between the variables were assessed using one-way ANOVA and multiple comparisons were adjusted by Bonferroni correction.

METHODS

Substrate fabrication

SLG was CVD grown on ultra-flat Cu surfaces and transferred, as previously described [1], onto SiO_2 and Si_3N_4 substrates for subsequent Raman and XPS characterization. Briefly, after annealing the Cu foil in a 400 sccm :100 sccm argon and hydrogen atmosphere at 100 mbar and 1015 °C, a SLG layer is nucleated at 15 mbar with 0.2 sccm methane and closed by successively increasing the methane content to 0.5 sccm. The graphene is transferred using PMMA (PMMA 950K A2, MicroChem, USA) or PS (Polystyrene MW ~192k, Sigma-Aldrich, USA). For neuronal culturing, SLG was transferred to glass coverslips or indium tin oxide (ITO). Before the transfer procedure, hosting substrates were ultrasonicated in acetone and isopropanol to assure the required cleanness. Glass and ITO coverslips followed an additionally cleaning step in concentrated HCl overnight. MLG sheets were CVD grown on Ni ultra-flat surfaces as described previously [2] and transferred on hosting substrates following the same procedure adopted for SLG. Briefly, the Ni foil was annealed as described before, at a temperature of 900 °C. After annealing, a methane flow of 10 sccm at 50 mbar enabled to the diffusion of carbon into the foil, which then, during the following slow cooling step, precipitated to a layer of MLG on the surface.

Gold samples have been prepared starting from glass rectangular slides (24 mm x 12 mm, 0.2 mm thick), cleaned previously in hot Piranha solution (H_2SO_4:H_2O_2, 5:5 ratio in volume) in order to remove eventually present organic contaminants. Subsequently, 15 nm of Au were thermally evaporated at a rate of 0.5 Å/s. A thin adhesion layer of 5 nm of Cr was used in order to improve Au/glass adhesion. A quartz crystal microbalance was used as thickness control.

To obtain suspended graphene structures, graphene is transferred on patterned substrates obtained using OrmoComp® (micro resist technology, GmbH), a flexible and biocompatible inorganic-organic material. The OrmoComp® substrates have been prepared on circular glasses (5 mm in diameter, 0.12 mm thick), previously cleaned in hot Piranha solution (H_2SO_4:H_2O_2 5:5 % v/v) in order to remove all organic contaminants. Subsequently, a poly-dimethylsiloxane (PDMS) master is prepared with replica molding process starting from a silicon stamp which is patterned with an array of parallel lines of width and periodicity of 10 μm and 20 μm, respectively. The PDMS master is used to press a drop of OrmoComp® on the circular glass in order to transfer the micropattern. Finally, the OrmoComp® is cured with UV light and the PDMS master is released. Commercially available single-layer CVD graphene on copper (GRAPHENEA – San Sebastián, Spain) is wet-transferred on the OrmoComp® substrates following the protocol described by Matruglio *et al.* [3]. Briefly, a layer of 250 nm of mr-I 7020 (a thermoplastic polymer of Micro Resist Technology GmbH) is used as sacrificial layer and spin coated on the graphene/Cu. The polymer/graphene/Cu membrane is placed in a copper etching solution ($FeCl_3$:H_2O 3:7 % v/v), etched overnight and finally washed in DI water in order to remove any residual due to the etching solution. The transfer of graphene is performed fishing the polymer/graphene/Cu membrane into the water directly on the OrmoComp® substrate. The water is left to evaporate at room temperature for 2 h, and mr-I 7020 is dissolved in cold acetone for 5 minutes. Critical point drying process is performed in order to avoid the collapse of the suspended structures.

Cell culture and electrophysiology

Isolation of primary brain tissue was carried out in accordance with the recommendations in the Guide for the Care and Use of Laboratory Animals of the National Institutes of Health and the appropriate international and institutional standards for the care and use of animals in research (Italian Ministry of Health, in agreement with the EU Recommendation 2007/526/CE). The protocols in this study and all performed experiments are approved by the local veterinary service and the institutional (SISSA) ethical committee, in accordance with the EU guidelines (2010/63/UE) and Italian law (decree 26/14).

Dissociated hippocampal cultures were obtained from neonatal rats (P0÷2) as previously described [4,5,6], and were plated on glass Control, SLG-, MLG- or Au-covered glass coverslips. As in our previous work with different carbon-based nanomaterial (e.g. carbon nanotubes, CNTs) [4,5,6], we did not pre-treat the culture substrates with any additional adhesion molecules, which might mask the effects of graphene. Cultured cells were incubated at 37 °C, 5% CO_2 in culture medium composed of Neurobasal-A (Thermo Fischer) containing B27 2% (Gibco) Glutamax 10 mM and Gentamycin 0.5 µM (Gibco), and used for experiments at 8÷10 days *in vitro* (DIV).

Somatic whole-cell patch clamp recordings were performed at room temperature (20÷22 °C) with pipettes (4÷7 MΩ) containing: 105 mM K gluconate, 20 mM KCl, 10 mM HEPES, 4 mM MgATP, 0.3 mM GTP, pH 7.35. The external saline solution contained: 150 mM NaCl, 4 mM KCl, 1 mM $MgCl_2$, 2 mM $CaCl_2$, 10 mM HEPES, 10 mM Glucose, pH 7.4. Under voltage-clamp mode we measured the neuronal passive membrane properties: input resistance and cell capacitance did not significantly differ between the four groups (in Control 592 ± 51 MΩ, 74 ± 5 pF, n = 47; in SLG 664 ± 57 MΩ, 83 ± 4 pF, n = 54; in MLG 614 ± 74 MΩ, 85 ± 5 pF, n = 18; in Au 656 ±

65 MΩ, 80 ± 6 pF, n = 17). In voltage-clamp experiments, the holding potential (V_h) was –56 mV, not corrected for liquid junction potential, that was calculated to be –14 mV in our experimental conditions; the uncompensated value for series resistance (Rs) was < 8÷11 MΩ.

Single spontaneous synaptic events (PSCs) and miniature PSCs (mPSCs) were detected by the use of the AxoGraph X (Axograph Scientific) event detection program and by the Clampfit 10 software (pClamp suite, Axon Instruments). On average, ≥ 400 events were analysed from each cell in order to obtain mean frequency and amplitude parameters. Glutamate AMPA-receptor and $GABA_A$-receptor mediated PSCs were isolated offline by building two templates with different kinetic parameters: respectively 0.1 ms rise-time; 3 and 30 ms decay time constant (τ); 10 and 100 ms template length. Previous work [6,7] indicated that in our experimental conditions, the vast majority of fast-decaying (τ < 5 ms) PSCs are mediated by the glutamate AMPA-receptor type; while the slow-decaying (τ > 20 ms) PSCs are mediated by the $GABA_A$-receptor type.

Current-voltage relations (I/V plots) were obtained by applying hyperpolarizing or depolarizing voltage steps (15 steps of ΔV = 10 mV; 500 ms duration) from –110 mV to + 30 mV (values corrected for liquid junction potential) in the presence of 1 μM Tetrodotoxin (TTX; Latoxan). A least square routine was fitted to the linear part of the I/V curve, the slope of which was used to calculate leak conductance. Assuming that a leak conductance is time and voltage independent, the I/V plot were corrected for leak currents by subtracting the observed currents from the extrapolated leak currents at the same level of test potential and the current values were then normalized to the cell capacitance [8].

In current-clamp recordings, bridge balancing was continuously monitored and adjusted. Action potentials (APs) were isolated off line by setting an appropriate threshold voltage (10 mV). The fast voltage transients that crossed this value were identified as APs and the spontaneous firing frequency for each neuron was calculated on a sample of at least 5 min of continuous recording keeping (by negative current injection) at –60 mV the resting membrane potential.

At –60 mV resting membrane potential, the AP properties were experimentally determined by depolarizing (from 0 to 200 pA, in 20 pA increments) current steps (500 ms). The first AP produced by the current-clamp series was used for single AP measurements, including amplitude, threshold, duration at half-amplitude and maximal rising slope [9,10,11]. The threshold for firing was determined by measuring the voltage at the upward deflection of the trace, maximal AP amplitude was measured from threshold to the peak of the spike, the duration was measured at half-amplitude from threshold to peak and the maximal rising slope was measured as max dV/dt in the selected area of the voltage tracings (all measures performed by Clampfit; pClamp suite, 10.2 version; Axon Instruments). From this analysis, no significant difference was found between Control (n = 21) and SLG (n = 19) groups (amplitude: 56.4 ± 3.5 mV for Controls and 59 ± 3.1 mV in SLG, P = 0.57; width: 3.5 ± 0.25 ms for Controls and 3.7 ± 0.38 ms for SLG, P = 0.59; threshold: –34.2 ± 1.5 mV Control and –35.5 ± 1.2 mV in SLG, P=0.34; maximal rise slope: 61.6 ± 7.5 mV/ms Control and 57.3 ± 5.8 mV/ms in SLG, P= 0.32).

In evoked APs, the AHP was quantified over a window of 100 ms by calculating the area below or above the voltage curve, starting 20 ms after the beginning of the AP. AP discharge patterns were investigated by delivering depolarizing current steps (1 s) of 200 pA while keeping the cells at –60 mV resting potential with steady

intracellular current injection. “Adapting” and “tonic” responses were identified as previously described [12].

Beside the monitoring of the spontaneous firing frequency, all the current clamp experiments were carried out in presence of the synaptic blockers (all from Sigma) CNQX (10 μM), Gabazine (5 μM) and APV (50 μM) added to the external solution. Current and voltage clamp responses were digitized at 20 kHz with the pCLAMP 10 software (Molecular Devices) and stored for further analysis.

Immunohistochemistry

Hippocampal neurons were fixed with 4% formaldehyde (prepared from fresh paraformaldehyde) in PBS for 20 min, permeabilized with 0.3% Triton-X-100 for 10 min and subsequently incubated with primary antibodies for 30 min at RT. After washing in PBS cultures were then incubated with secondary antibodies for 45 min and then mounted in *Vectashield* (Vector Laboratories) on 1 mm thick microscope glass slides. As primary antibodies were used rabbit polyclonal anti-β-tubulin III (Sigma T2200, 1:250 dilution), mouse monoclonal anti-GFAP (Sigma-Aldrich, 1:200 dilution), and guinea pig anti-vesicular glutamate transporter 1 (VGLUT1; Millipore, 1:2000). As secondary antibodies were used Alexa 594 goat anti rabbit (Invitrogen, dilution 1:500), Alexa 488 goat anti mouse (Invitrogen, dilution 1:500), and Alexa 488 goat anti guinea-pig (Invitrogen, 1:500). To stain cells nuclei, we used DAPI (Invitrogen, 1:200 dilution). To quantify cell density, images were acquired with an Epifluorescence Microscope (DM 6000, Leica; 10× objective). We collected 10 fields (1000 μm × 500 μm) per coverslip and analysed fluorescence signals using ImageJ software (http://rsb.info.nih.gov/ij/).

To evaluate the orientation of the re-growing axons on the various substrates, we quantified their relative orientation based on the directionality analysis [13]. Briefly, the mean fibre's relative dispersion was computed from n = 5 randomly sampled images per condition (Control, SLG, MLG and Au) where neuronal processes were visualized by class III β-tubulin immunofluorescence (Fig. 2a). The analysis was carried out using the Directionality plugin of Fiji software inferring the preferred orientation of "structures" present in the input image. Fibre orientation was calculated via a Fourier component analysis. We found no significant differences in the direction of the mean fibre's dispersion among different conditions (Control = 30 ± 9°; SLG = 29 ± 7°; MLG = 38 ± 8°; Au = 35 ± 9°) indicating a negligible impact of the substrate on the orientation of the neuronal processes.

To quantify VGlut1 puncta, n = 20 ± 10 z-stacks (acquired every 0.4 μm) were taken from n = 10 randomly selected fields (160 μm × 80 μm) per coverslip using an inverted confocal Microscope (Nikon Eclipse Ti-E; 40x oil immersion objective, 1.3 NA). We selected only VGlut1-positive puncta (< 2 μm^3) colocalized with β-tubulin III positive signal. For each image VGlut1 puncta were normalized to the β-tubulin III positive volume. Images were analysed using the Volocity software (Perkin Elmer).

To highlight GABAergic neurons, cultures were stained with anti-GABA polyclonal primary antibody produced in rabbit (SIGMA, A2052: 1:500). To label the NKCC1 co-transporter, we used anti NKCC1 rabbit polyclonal primary antibody (Abcam; AB59791; 5 μg/mL). Cultures were then stained with class III β-tubulin primary antibody produced in mouse (SIGMA; T5076; 1:500). As secondary antibody, we used AlexaFluor 488 goat anti rabbit (ThermoFisher A11034; 1:500), and AlexaFluor 594 goat anti mouse (ThermoFisher, A11032; 1:500).

To quantify the percentage of GABA-positive neurons, 10 ± 5 confocal z-stack (Nikon PlanFluor 40× / 1.3 NA) were acquired from randomly selected fields and GABA-positive neurons were counted. This value was then normalized to the overall number of neurons (class III β-tubulin positive cells) for each field. To quantify NKCC1 puncta, n = 10 z-stacks (acquired every 0.25 μm) were taken from selected fields (106 μm × 106 μm) each group, using an inverted confocal Microscope (Nikon Eclipse Ti-E; Nikon Plan Apo Lambda 60x oil immersion objective, 1.4 NA). To quantify the amount of neuron-related NKCC1, only NKCC1-positive puncta in contact with the β-tubulin III signal were selected.

Imaging

For Cl^- imaging experiments, primary hippocampal cultures (DIV 8÷10) were loaded with the fluorescent Chloride indicator MQAE (Abcam; ab145418) diluted in the standard extracellular solution at a final concentration of 1 mM for 10 min at 37 °C in the cell culture incubator. Samples were then washed in the extracellular solution for 10 min at 37 °C. Samples were placed in a recording chamber mounted on an inverted microscope (Nikon Eclipse Ti-U) and observed with a 60× objective (0.7 NA, PlanFluor, Nikon). Images (1024 × 1024 pixels) from fields containing 7 ± 4 neurons were acquired for 2 minutes at Hz by a Hamamatsu Orca-Flash 4.0 digital camera, exciting the MQAE dye at the 365 nm Hg peak using a UV-2A Nikon filter set. Excitation light was attenuated by a neutral density filter (ND 16). Images of emitted fluorescence (>420 nm) were displayed on a colour monitor controlled by an integrating imaging software package (HCImage, Hamamatsu) using a personal computer. Recorded images were analysed offline with the Clampfit software (pClamp suite, 10.2 version; Axon Instruments). Image

time stacks were analysed in selected region of interest (ROI) to measure the variations in MQAE fluorescence intensity. Intracellular Cl^- transients were expressed as fractional amplitude variations ($\Delta F/F_0$, where F_0 is the baseline fluorescence level and ΔF is the change over the baseline); the onset time of neuronal activation determined by detecting those events in the fluorescence signal that exceed at least five times the standard deviation of the noise. To elicit chloride influx/efflux through the membrane, an injection pipette (patch pipette with resistance of 1÷4 MΩ, filled with 10 mM GABA diluted in the extracellular solution) was positioned at 20÷50 µm from the cell soma and connected to a pico-spritzer (PDES-02DX, npi Electronics) with 1 psi in-line pressure. 500 ms GABA puffs were delivered at fixed times. At the beginning of each experiment, a pipette containing pure saline was used to exclude artefacts due to the pressure injection (Supplemental Fig. S2). We found an overall percentage of 37 ± 6.5 % Control neurons and 35.6 ± 9.3 % SLG neurons that did not respond to the stimulation, and were excluded from further analysis.

Electron microscopy (EM)

Scanning EM imaging was conducted using collecting secondary electrons on a Gemini SUPRA 40 SEM (Carl Zeiss NTS GmbH, Oberkochen). Before SEM imaging, neuronal cells grown on the different substrates were fixed in 3% Glutaraldehyde in 0.1 M Sodium Cacodylate Buffer (pH 7.4), then dehydrated sequentially in ethanol solutions of 50, 75, 95, 99 and 100% (vol/vol in H_2O, 3 minutes each, 4 °C). After overnight drying in the fridge, and before imaging, samples were metalized with a 5 nm thick layer of platinum-iridium alloy using a

metal sputter coater (Polaron SC7620). In order to prevent electron induced surface charging, low accelerating voltages (1÷3 keV) were used for cells visualization. SEM images of cells cross sections at membrane-substrate interface were obtained by focused ion beam (FIB) using a LEO-ZEISS Cross-Beam 1540 XB system. Gallium ion beam milling was performed with a current beam of 30 mA while SEM images were collected at 3 kV. Samples were prepared following the same procedure described in the previous paragraph.

Substrate characterization

AFM topography data (MFP-3D, Asylum Research, Santa Barbara, California, USA) was acquired in tapping mode, using silicon cantilevers in ambient conditions. The roughness estimates were calculated using the standard deviation of elevation in mapped surface areas with sizes of 10 µm x 10 µm. XPS spectra were recorded in ultra-high vacuum conditions using a monochromatic SPECS XR-50 Mg Kα X-Ray source ($E_{K\alpha}$ = 1253.6 eV) and a hemispherical energy analyser (Phoibos 100/150, Specs, Berlin, Germany). µ-Raman spectra were recorded with an in-house built system using an Ar-ion laser at 514.5 nm and operating with a spectral resolution of 0.75 cm^{-1}.

Raman measurements in aqueous conditions have been carried out at on the IUVS beamline at Elettra synchrotron radiation facility (Trieste, Italy). A complete description of the experimental apparatus can be found elsewhere [10.1016/j.nima.2012.11.037]. A 532 nm laser source, with a beam power near 5 mW, has been employed as excitation source. The scattered radiation was collected in a backscattering geometrical configuration. Slight modifications on the standard backscattering set-up have been introduced to allow measurements in liquid

conditions (see Supplementary Methods). A 750 mm focal length Czerny-Turner spectrometer, equipped with an holographic reflection grating of 1800 g/mm and coupled with a Peltier-cooled back-thinned CCD, has been used to get the final Raman spectra.

Data Analysis, Statistics and Reproducibility

All values from samples subjected to the same experimental protocols were pooled together and expressed as histograms (mean ± SEM with n = biologically independent experiments, usually number of cells, unless otherwise indicated) or through box-plot representation when one or more data set were found to follow a non normal distribution. In box-plots, the thick horizontal bar indicates the median value, the boxed area extends from the 25^{th} to 75^{th} percentiles while whiskers from the 5^{th} to the 95^{th} percentiles. The homogeneity of variances was assessed through the Levene's test.

Statistically significant difference between two data sets was assessed by Student's t-test for parametric data and by Mann-Whitney for non-parametric ones. Differences between the logarithmic values of the analysed variables were assessed using one-way ANOVA [14] and multiple comparisons were adjusted by Bonferroni correction. Statistical significance was determined at $P < 0.05$, unless otherwise indicated. Significance was graphically indicated as follows: * $P < 0.05$, ** $P < 0.01$, *** $P < 0.001$.

Mathematical models of single neurons and neuronal networks

Full details on the mathematical models are reported in the Supplementary Information.

REFERENCES FOR METHODS

[1] Drieschner, S. et al. Frequency response of electrolyte-gated graphene electrodes and transistors. Journal of Physics D: Applied Physics 50, 095304 (2017).

[2] Drieschner, S. et al. High surface area graphene foams by chemical vapor deposition. 2D Materials 3, 045013 (2016).

[3] Matruglio, A. et al. Contamination-free suspended graphene structures by a Ti-based transfer method Carbon, 103, 305-310 (2016).

[4] Lovat, V. et al. Carbon nanotube substrates boost neuronal electrical signaling. Nano Lett. 5, 1107-1110 (2005).

[5] Cellot, G. et al. Carbon nanotubes might improve neuronal performance by favouring electrical shortcuts. Nat. Nanotechnol. 4, 126-133 (2009).

[6] Cellot, G. et al, Carbon nanotube scaffolds tune synaptic strength in cultured neural circuits: novel frontiers in nanomaterial-tissue interactions. J. Neurosci. 31, 12945-12953 (2011).

[7] Pampaloni, NP. et al. Sculpting neurotransmission during synaptic development by 2D nanostructured interfaces. Nanomedicine. S1549-9634, 30082-5 (2017).

[8] Sontheimer, H. & Ransom, C. Whole-Cell Patch-Clamp Recordings. Neuromethods 35, 35-67 Humana Press Inc., (2007).

[9] Ruscheweyh, R. & Sandkuhler, J. Lamina-specific membrane and discharge properties of rat spinal dorsal horn neurones in vitro. J Physiol. 541, 231-244 (2002).

[10] Chang, YM. & Luebke, JI. Electrophysiological diversity of layer 5 pyramidal cells in the prefrontal cortex of the rhesus monkey: in vitro slice studies. J Neurophysiol. 98, 2622-32. (2007)

[11] Renganathan, M., Cummins, TR. & Waxman, SG. Contribution of Na(v)1.8 sodium channels to action potential electrogenesis in DRG neurons. J Neurophysiol. 86, 629-40 (2001).

[12] Furlan, F. et al. ERG conductance expression modulates the excitability of ventral horn GABAergic interneurons that control rhythmic oscillations in the developing mouse spinal cord. J. Neurosci. 27, 919-928 (2007).

[13] Usmani S, et al. 3D meshes of carbon nanotubes guide functional reconnection of segregated spinal explants. Sci Adv. e1600087 (2016).

[14] Wilcox RR & Rousselet GA. A Guide to Robust Statistical Methods in Neuroscience. Curr Protoc Neurosci. 82, 8.42.1-8.42.30 (2018).

Additional information

Supplementary information, results and figures are available in the online version of the paper. Correspondence and requests for materials should be addressed to Denis Scaini dscaini@sissa.it; Josè Antonio Garrido joseantonio.garrido@icn2.cat; Laura Ballerini laura.ballerini@sissa.it

Data availability

The data that support the plots within this paper and other findings of this study are available from the corresponding authors upon reasonable request. The mathematical model is available online at ModelDB (https://senselab.med.yale.edu/ModelDB/).

Fig. 1

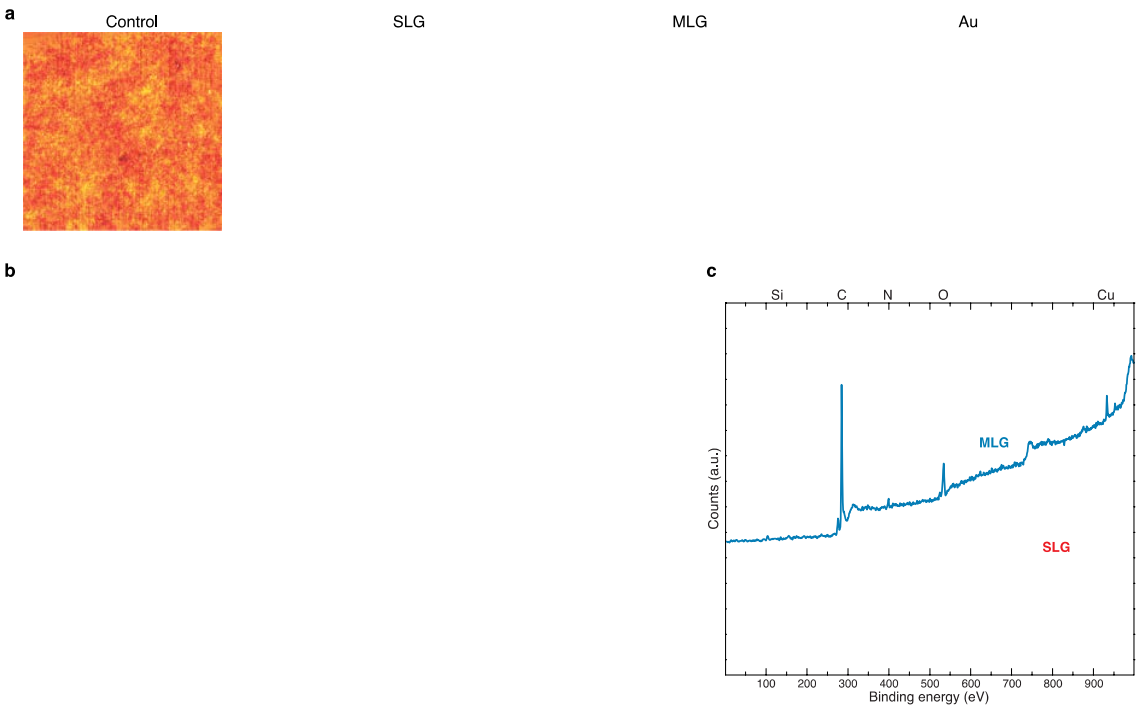
a
Control
SLG
MLG
Au
b
c
Si
C
N
O
Cu
MLG
SLG
Counts (a.u.)
100
200
300
400
500
600
700
800
900
Binding energy (eV)

Fig. 2

a

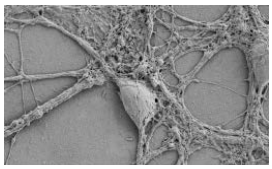

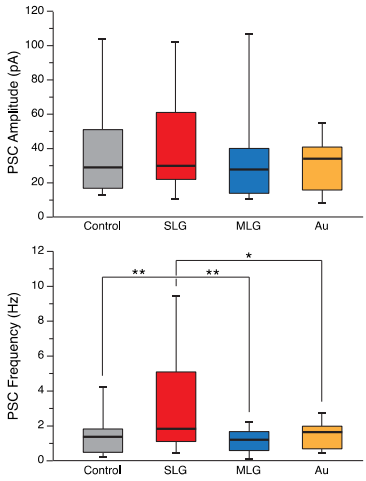
PSC Amplitude (pA)
120
100
80
60
40
20
0
Control
SLG
MLG
Au
PSC Frequency (Hz)
12
10
8
6
4
2
0
**
**
*
Control
SLG
MLG
Au

Fig. 3

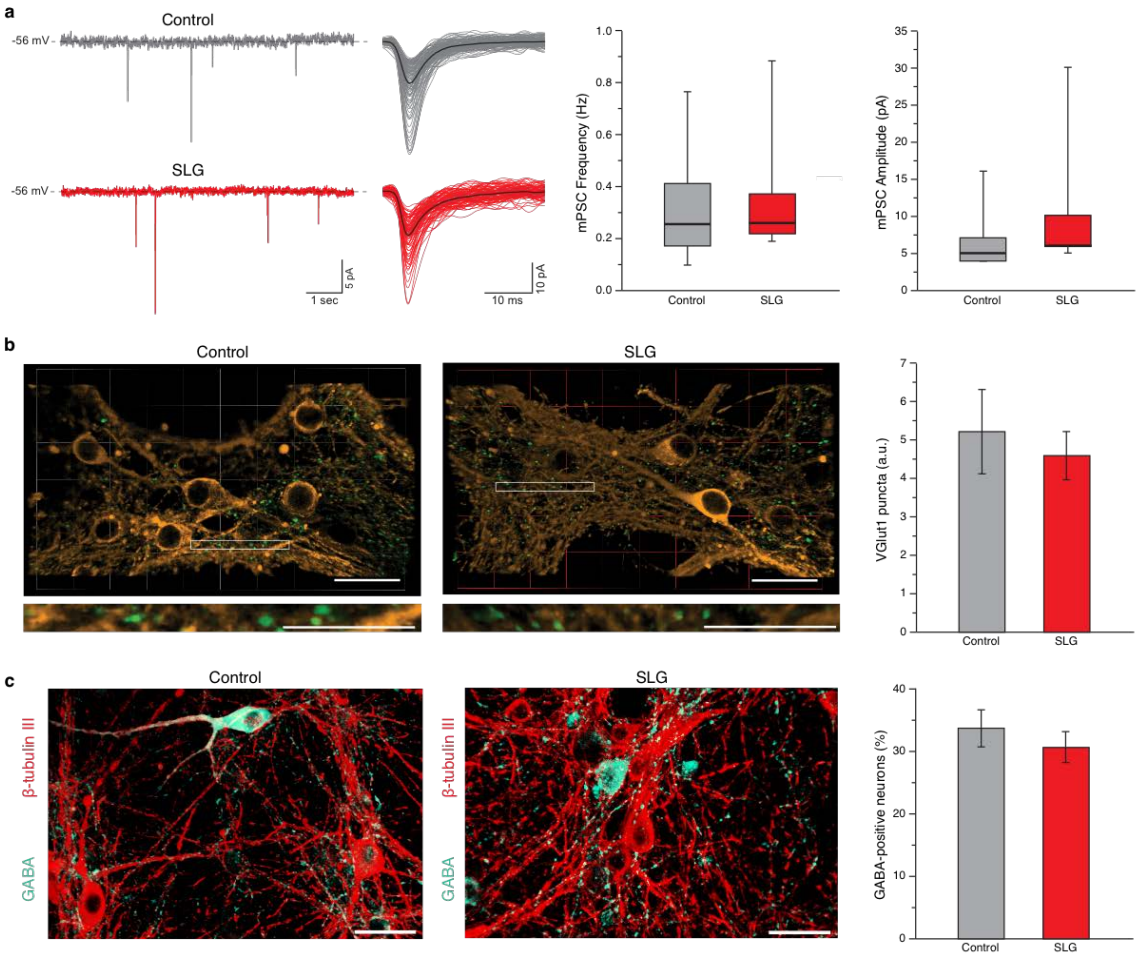
a
Control
-56 mV
SLG
-56 mV
1 sec
5 pA
10 ms
10 pA
mPSC Frequency (Hz)
Control
SLG
mPSC Amplitude (pA)
Control
SLG
b
Control
SLG
VGlut1 puncta (a.u.)
Control
SLG
c
Control
SLG
β-tubulin III
GABA
β-tubulin III
GABA
GABA-positive neurons (%)
Control
SLG

Fig. 4

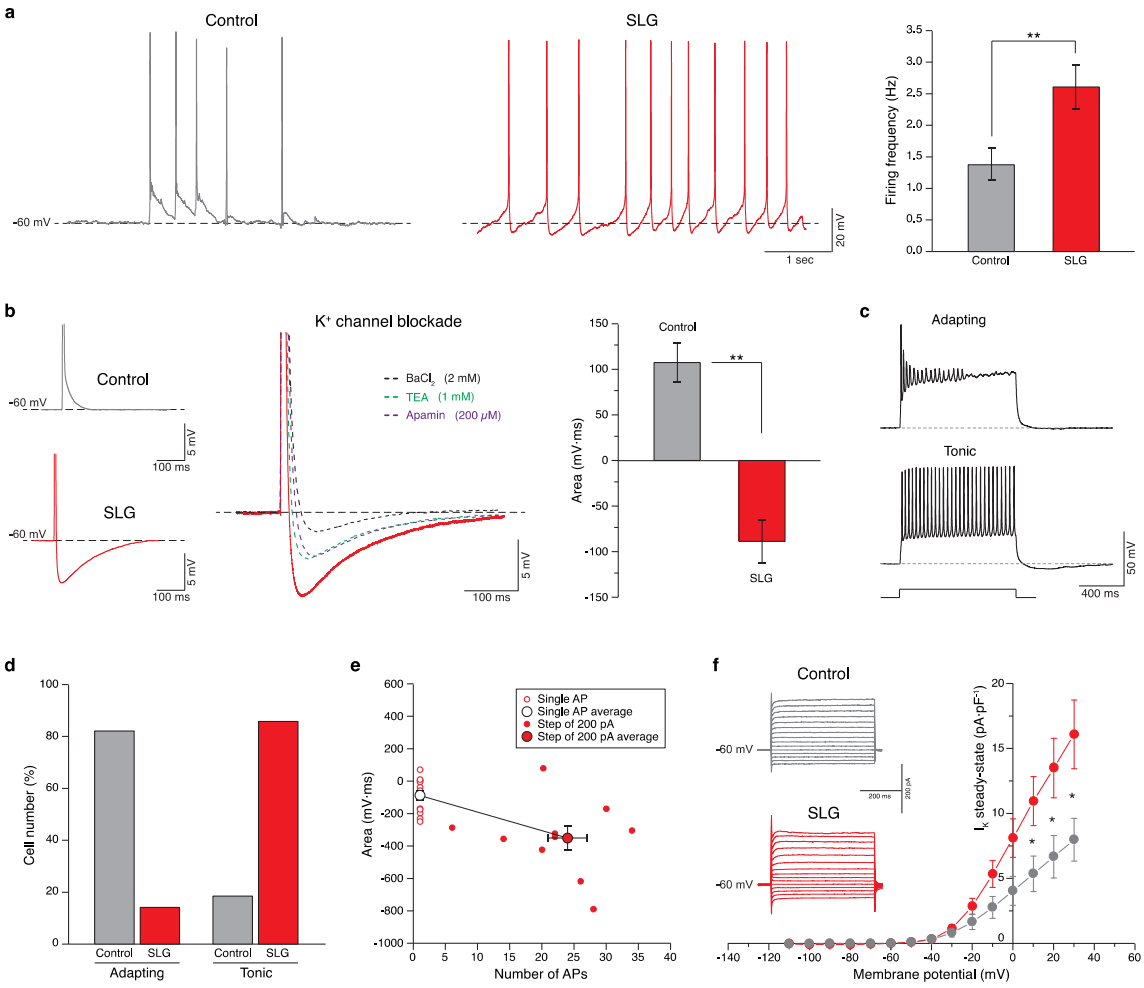
a
Control
SLG
-60 mV
20 mV
1 sec
Firing frequency (Hz)
Control
SLG
b
Control
SLG
K⁺ channel blockade
BaCl2 (2 mM)
TEA (1 mM)
Apamin (200 μM)
Area (mV·ms)
c
Adapting
Tonic
50 mV
400 ms
d
Cell number (%)
Control
SLG
Adapting
Tonic
e
Single AP
Single AP average
Step of 200 pA
Step of 200 pA average
Area (mV·ms)
Number of APs
f
Control
SLG
Membrane potential (mV)

Fig. 5

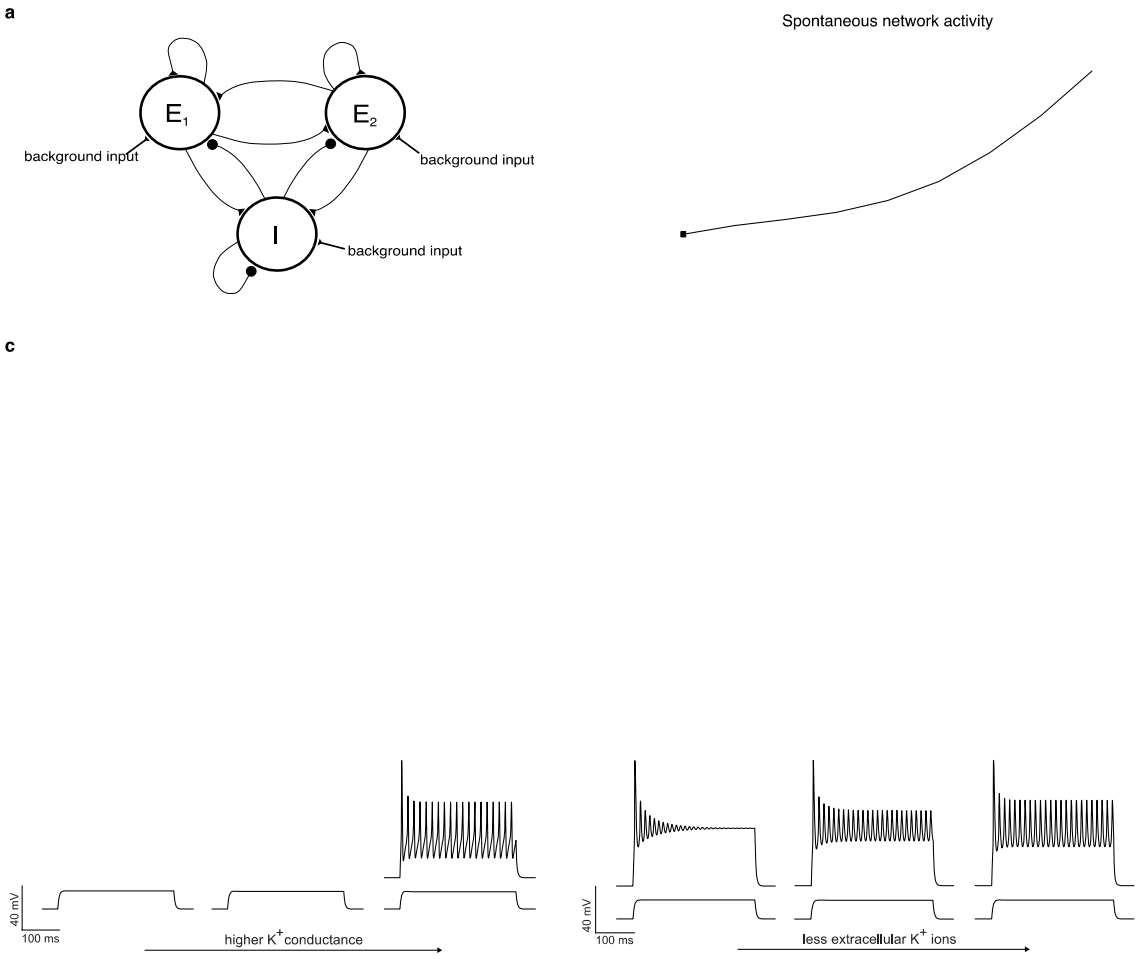
a
E1
E2
I
background input
background input
background input
Spontaneous network activity
c
40 mV
100 ms
higher K+ conductance
40 mV
100 ms
less extracellular K+ ions

Fig. 6

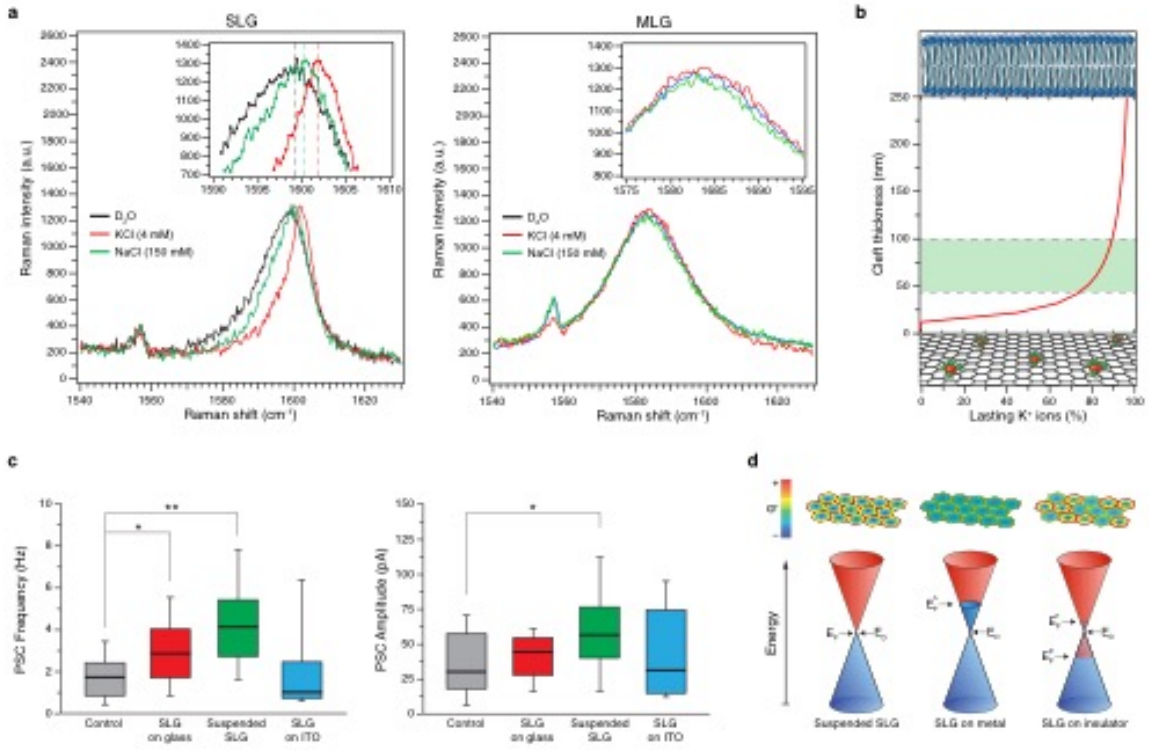
a
SLG
MLG
Raman intensity (a.u.)
Raman shift (cm⁻¹)
D2O
KCl (4 mM)
NaCl (150 mM)
b
Graft thickness (nm)
Lasting K+ ions (%)
c
PSC Frequency (Hz)
PSC Amplitude (pA)
Control
SLG on glass
Suspended SLG
SLG on ITO
d
Energy
Suspended SLG
SLG on metal
SLG on insulator